Supporting Information

Alden et al. 10.1073/pnas.1309394110

Dark-Field Transmission Electron Microscopy and Composite Order-Parameter Vector Images from [−2110] Diffraction Spots

As stated in the main text, if an aperture is placed in the diffraction plane at one of the angles corresponding to planes of atoms along the zigzag direction (the [−1010] family of diffraction angles), then at nonzero sample tilt AB and BA are no longer symmetric with respect to the beam axis, and one phase appears bright whereas the other is dark (1).

To image the AB/BA soliton boundaries on a few-micrometers scale, we apply the same technique, only instead of using the "inner" [−1010] diffraction spots, we use the aperture to select the "outer" diffraction spots—the [−2110] family of diffraction angles. For this family, in which electrons scatter from planes parallel to a given armchair direction, if a boundary translation, $\boldsymbol{\Delta u}$, has a component perpendicular to that armchair direction, its contrast will change relative to the adjacent Bernal-stacked regions. Fig. S1 *A*–*C* displays a series of dark-field transmission electron microscopy (DF-TEM) images of the sample in Fig. 1 *C* and *D*. Fig. S1*F* is taken directly from Fig. 1*C*, whereas in Fig. S1 *A*–*C* we have used an aperture to select three different [−2110] angles, indicated by the circles in Fig. S1*E*. Comparing each of the boundary images, Fig. S1 *A*–*C*, to the domain image, Fig. S1*F*, we notice that one-third—and a different third—of the boundaries in each image, Fig. S1 *A*–*C*, is invisible. From this we infer that the interlayer translation occurring across a given invisible boundary is precisely along the armchair direction that corresponds to the diffraction angle through which the image was taken. We indicate these boundaries schematically by dashed lines in Fig. S1 *A*–*C* and *F*. Thus, each boundary represents a single-bond-length interlayer translation, in agreement with what we might expect by examining Fig. 1*A*, where the minimal-energy path connecting AB to BA through a saddle point corresponds to translation along one of three armchair directions.

Fig. S1*D* shows a composite image in which we have colored the images from each of the three [−2110] diffraction spots, Fig. S1 *A*–*C*, red, blue, and green, respectively, and merged them to create the image shown (in a manner identical to that used for Figs. 1*D* and 2*A*). In this image, each boundary has a color corresponding to the order parameter vector, $\boldsymbol{\Delta u}$, indicated by arrows in Fig. S1*D* and Fig. 1*D*. Moving across the sample in Fig. 1*D* from left to right, the density of boundaries decreases, from 1 per 6 nm to 1 per 90 nm, corresponding to a decrease in relative global twist from 1.4° to 0.1°, which we posit occurred as a gradual interlayer rotation-relaxation process during the chemical vapor deposition (CVD) growth from left to right.

Linear Global Interlayer Strain Example

The "rotational interlayer strain" sample in Figs. 1 and 2 has a striking and easily interpreted structure, but is not the most common type of sample. Among tens to hundreds of samples imaged, we saw this sort of hexagonal/triangular pattern only four times. More typically, interlayer strain is less regular, often exhibiting some global interlayer uniaxial strain—likely related to the terraced structure in the copper growth substrate (1). An example of such a uniaxially strained case is shown in Fig. S2. Fig. S2*A* is an "AB/BA domain" image, taken from a [−1010] diffraction angle, whereas Fig. S2*B* is a composite "boundary" image generated from the [−2110] family of diffraction angles as described for Fig. S1*D* and Figs. 1*D* and 2*A* above and in the main text.

In the case of this sample, the bilayer accumulates interlayer strain across the sample vertically. The translations having a significant shear component (red and green) largely cancel out, leaving an accumulation of strain, primarily due to the nearly pure-strain boundaries (blue). Two subtleties in this latter case are worth noting. First, owing to the energy landscape, a sample with large relative interlayer strain globally will always have some locally sheared boundaries, because this is the only way to accumulate strain while avoiding a translation through an energetically unfavorable AA stacking (Fig. 1*A*). Second, there are some interesting topological features in this sample that cannot be explained by the presence of interlayer strain and shear between two stacked sheets of pristine graphene, but instead arise from topological point defects having nonzero in-plane Burger's vector.

For the interested reader, one of these features is highlighted in the insets to Fig. S2. Notice that two different translation vectors, $\boldsymbol{\Delta u}$ (red and blue lines), are associated with the boundary between a single AB- and single BA-stacked region. If the two layers in the bilayer were pristine graphene, the order parameter vector, $\boldsymbol{u}$, we would assign to the BA region based on the known shift at the red boundary would be inconsistent with that assigned based on the blue boundary. One explanation for this apparent inconsistency is that one of the two layers is missing a (zigzag) line of atoms, and has been stitched together with an offset that directly corresponds with the difference between the vectors associated with the red and blue domain boundaries. Or, stated another way, there is a point defect at the intersection of the red and blue lines having a nonzero Burger's vector. This type of defect appears in many of our CVD-grown samples. In this image alone, there are more than 10 such defects. (For those interested in imaging such defects with atomic resolution, this DF-TEM technique is useful for quickly identifying, to within ∼10 nm, where to look. In attempting to image some of these defects ourselves, we found that of ∼10 that we tried to image with atomic resolution, all were covered with polymethyl methacrylate/etchant residue, perhaps owing to increased reactivity.)

Averaging and Cross-Correlating Images for Fig. 2

In Fig. 2 *C* and *D*, respectively, three and seven frames were cross-correlated and averaged, after applying a 0.2-Å low-pass filter. Fig. S3 *A* and *B* show examples of the raw images from which, respectively, Fig. 2 *C* and *D* were taken. The cross-correlation was done using Matlab's image processing toolbox, in a two-pass registry. The first pass registered all images to the first frame in the stack, and the second registered all images, including the first, to the average registered image from the first pass. After the second pass, the registered images were averaged, and the grayscale was adjusted to increase the contrast. The low-pass filter applied to the images was a standard Gaussian filter with $\sigma = 0.2$ Å.

Simulated Scanning TEM Images and Soliton Model

To simulate the scanning TEM (STEM) images presented in Fig. 3, we used E. J. Kirkland's multislice code, as described in *Methods* in the main text. The atomic coordinates in the simulated image (and also in the schematics) were specified by using the two-chain Frenkel–Kontorova model (2) to describe the interlayer translation, $\boldsymbol{\Delta u}$, in the boundary region in terms of the sine-Gordon equation:

$$\frac{ka^2}{4}\frac{\partial^2 \boldsymbol{\Delta u}}{\partial x^2} = \frac{\pi}{2} V_{sp} \sin(2\pi \boldsymbol{\Delta u}).$$

Here, k is the stiffness and V_{sp} is saddle-point energy in Fig. 1*A*, a = 0.141 nm is the bond length in graphene, and $\boldsymbol{\Delta u}$ is the broken symmetry-order parameter, which varies from 0 to 1 across the boundary region. The first term is elastic energy stored in the boundary region, and the final term is the misalignment cost associated with non-AB/BA stacking.

This equation has soliton "kink" and "anti-kink" solutions of the form

$$\boldsymbol{\Delta u}_{\pm} = \frac{1}{2} \mp \frac{1}{2} \pm \frac{2}{\pi} \arctan\left(\exp\left(\frac{2\pi}{a} \sqrt{\frac{V_{sp}}{k}} x \right) \right).$$

The equilibrium width, $w_{eq} = \frac{a}{2}\sqrt{k/V_{sp}}$, was used as a fitting parameter to match the FWHMs of the simulated images with those of the STEM images in Fig. 3. Upon obtaining the multislice output, a Gaussian low-pass filter (σ = 0.04 nm) was applied to the simulated image to represent the incoherent probe size, again choosing this value based on a match with the STEM images.

STEM FWHM

To improve the signal-to-noise for our atomic resolution images, the composite images in Fig. 3 were generated by averaging three to four regions in a single image that were adjacent to each other along the soliton. The raw images are shown in Fig. S4 *A* and *B* for Fig. 3 *A* and *D*, respectively. The fits to the composite images in Fig. 3 yielded FWHM of 13 and 5.9 for strain and shear, respectively. However, owing to small motions of the soliton during imaging and slight in-plane curvature in the soliton, this averaging procedure leads to an apparent broadening of the soliton's width.

To avoid such broadening when determining the widths for Fig. 3 and thus parameters of the soliton model (and also the cited "average FWHM" for shear and strain boundaries), we use a second procedure for all STEM soliton width measurements. We fit Gaussians to line-cuts in the raw images parallel to the scan direction—averaging every 2–10 lines, depending on the size of the image—which eliminates the majority of the broadening due to fluctuations or curvature seen in the above averaging procedure. For Fig. S4, these cuts were in the horizontal direction. For the Gaussian fits, we used the center, μ, height, A, and width, σ, as fitting parameters, and fixed the base of the Gaussian to be the average intensity of a region as far from the boundary as possible within the same image. Fits either having μ within 1 σ of the edge of the image, or having a larger-than-median rmse were discarded. The resulting FWHMs from these fits were multiplied by the cosine of the angle between the scan direction and the boundary to obtain the boundary FWHMs. The error bars in Fig. 3*H* are ±1 SD in the fitted width of a given soliton across all scan lines.

Relating STEM FWHM to Sine-Gordon

To determine the soliton parameters based on our FWHM measurements we needed a way to relate the soliton width parameter to the FWHM. We accomplished this by fitting a polynomial function of $\boldsymbol{\Delta u}$ (the change in the order parameter) to the average intensity across the multislice simulated STEM images in Fig. 3. Because the coordinates of the atoms were generated using the solution to the soliton equation (discussed above) this enables us to fit a polynomial in $\boldsymbol{\Delta u}$ that we can use to relate FWHM to soliton the width. For $\boldsymbol{\Delta u}$ between 0 and 1, we find that the following polynomial fitted the multislice image well—and, indeed, had lower rmse than a Gaussian fit:

$$I(z) = Az^3 + Bz^2 + Cz + D.$$

Here, $z = (\boldsymbol{\Delta u} - 1/2)$ (2), and A–D are fitted parameters, having respective values of −25.8169, 4.7742, 1.7676, and 0.6628. Fitting a Gaussian to this function for a few values of the soliton width (recall that $\boldsymbol{\Delta u}$ is a function of the soliton width) allows us to establish a linear relationship between FWHM and soliton width:

$$w_{soliton} \equiv \frac{a}{2}\sqrt{\frac{k}{V_{sp}}} = A_1 w_{FWHM} + A_0.$$

The fitted values for A_1 and A_0 are, respectively, 1.458 and 0.099. Using this relationship enables us to extract physical constants from our STEM measurements of the soliton's FWHM.

DF-TEM Width vs. Angle

To image soliton boundaries in a larger number of samples, and on an approximately micrometer-length scale, we use DF-TEM. We find very little preference for any one angle over the others, with many samples exhibiting boundaries at all angles. Fig. S5 displays the boundary width vs. angle ϕ obtained via DF-TEM. As was seen for the STEM measurements in Fig. 3*H*, the soliton width varies approximately sinusoidally with angle, having a maximum FWHM at 0° (and 180°), corresponding to purely tensile solitons, and decreasing to a minimum at 90°, corresponding to purely shear solitons. The solitons appear wider than those measured by STEM, and have greater variability. This is likely the result of variations in the corrugations and built-in strain in the samples—to which width measurements performed using DF-TEM are more susceptible than those using STEM, where corrugated samples can easily be identified and rejected. In particular, corrugations parallel to a tensile boundary are expected to decrease the equilibrium width of the boundary while increasing its measured width, because the out-of-plane-tilted bilayer is difficult to distinguish from the interlayer-translated bilayer for small angles/translations. We find that as the number of supporting graphene layers—i.e., graphene layers oriented at some angle (>2°) with respect to the bilayer—increases from 0 to 2, shown in Fig. S5 *A*–*C*, respectively, the measured FWHM and the variability in FWHM measurements is reduced. This supports the view that corrugations are responsible for the variability in and broadening of measured soliton width, because the increasing stiffness associated with an increasing number of supporting layers reduces the amplitude of corrugations. With two supporting layers, the model fits well, and the measured strain soliton-FWHM is ∼11 nm and the measured tensile soliton-FWHM is ∼6 nm, in excellent agreement with our STEM measurements.

Relating DF-TEM FWHM to Sine-Gordon

The DF-TEM fits to the soliton width-vs.-angle model are treated similarly to those for STEM. In DF-TEM, the intensity collected through a [−2110] diffraction spot, at normal incidence, relates to the interlayer translation as

$$I(\boldsymbol{\Delta u}) \propto \cos^2(\boldsymbol{\Delta u}).$$

Because the resolution of this technique is significantly below that of STEM, we must take into account the broadening of a soliton by its convolution with the finite-sized electron beam. In the case of resolution broadening, the soliton FWHM will be given by

$$w_{FWHM} = 2\sqrt{2\log 2\left(\sigma^2_{measured} - \sigma^2_{resolution}\right)}.$$

We determine the resolution, $\sigma_{resolution}$, by, for each image, measuring the resolution broadening of a graphene edge (often a

bilayer–monolayer step), which we assume to be atomically sharp. We treat the image of the edge as the convolution between a Heaviside function and a Gaussian probe and extract the width parameter, σ, for such a probe.

We automate the finding and fitting of the solitons in our outer-diffraction spot DF-TEM images. Our algorithm first finds the boundaries, primarily by applying a threshold to the image, and assuming all pixels darker than a given threshold are soliton pixels. We then determine the orientation of the boundary by finding the ∼20- × 20-pixel mask that minimizes the sum of squares between the image and mask, where the masks consist of a dark line drawn at some angle on a light background. We throw out error-prone regions (such as regions where two solitons intersect). We then fit a Gaussian at each soliton pixel, in a direction perpendicular to the soliton, averaging over the adjacent three pixels on either side, parallel to the soliton. Because some of the found pixels are not in fact solitons, and result in Gaussian fits with extremely large sigma (i.e., a flat region), we use the median width at each angle (rather than the mean) so as not to be strongly affected by such outliers.

Finally, we use the linear empirical relationship between the FWHM of $I(\boldsymbol{\Delta u})$ and the sine-Gordon width to relate the fitted Gaussians to the sine-Gordon width.

1. Brown L, et al. (2012) Twinning and twisting of tri- and bilayer graphene. *Nano Lett* 12(3):1609–1615.

2. Popov AM, Lebedeva IV, Knizhnik AA, Lozovik YE, Potapkin BV (2011) Commensurate-incommensurate phase transition in bilayer graphene. *Phys Rev B* 84:045404.

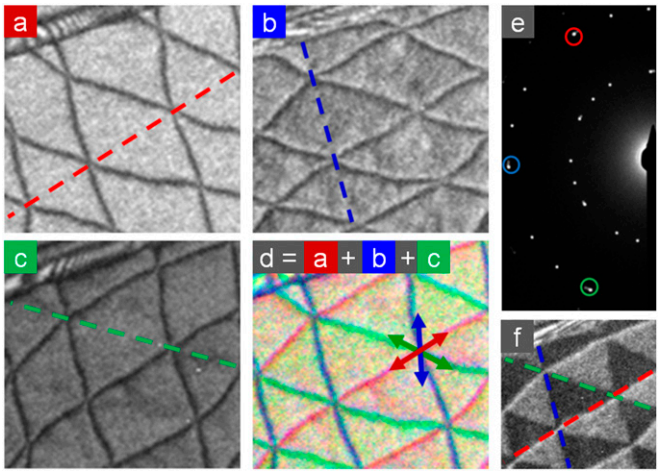

Fig. S1. Composite-image construction. (*A*–*C*) DF-TEM images taken through apertures in the diffraction plane, as indicated by the similarly colored circles in *E*. In each image two of the three domain boundaries are visible. The "missing" boundary in each (dashed lines) corresponds to a boundary with interlayer translation parallel to the diffraction planes being imaged. (*D*) Composite image constructed by coloring *A*–*C* red, blue, and green, respectively, and summing. (*E*) Diffraction image for this sample, showing the locations of the apertures used for imaging *A*–*C*. (*F*) DF-TEM image of the sample in *A*–*F* taken through one of the "inner" [−1010] diffraction spots, indicating the locations of AB and BA domains.

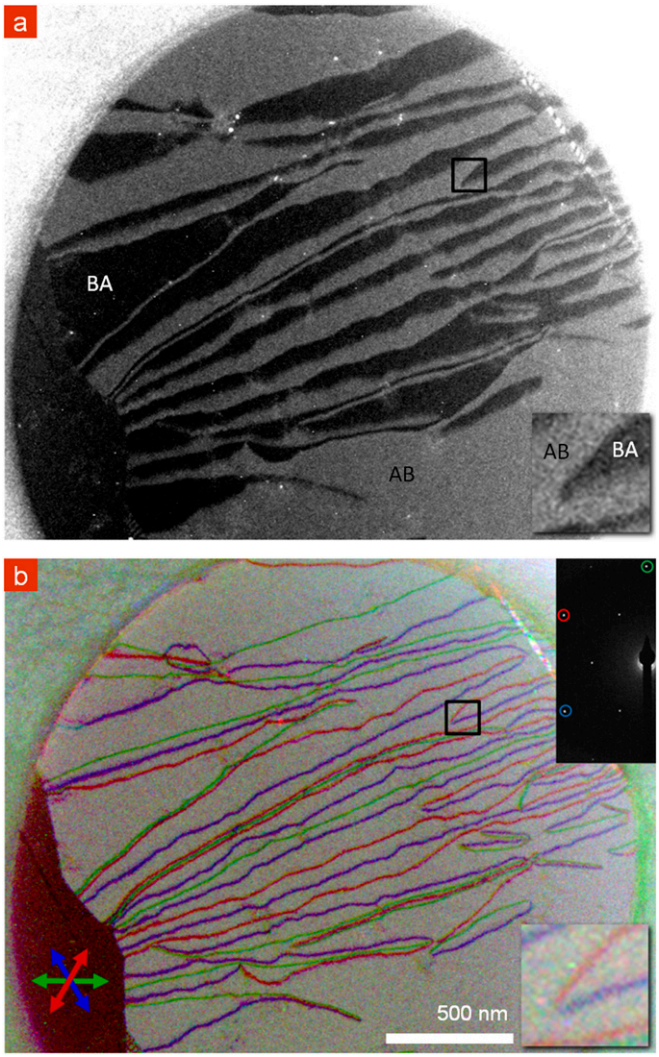

Fig. S2. Example of a bilayer sample exhibiting predominantly linear global strain. (*A*) DF-TEM image taken from one of the [−1010] diffraction angles showing lines of alternating AB- and BA-stacked graphene. (*B*) Composite DF-TEM image taken from [−2110] angles, using the same methods as those used for Fig. 1*C*, coloring the soliton boundaries according to their interlayer translation vectors, $\boldsymbol{\Delta u}$, as indicated by the arrows. Insets highlight an interesting defect, as discussed in *Supporting Information*.

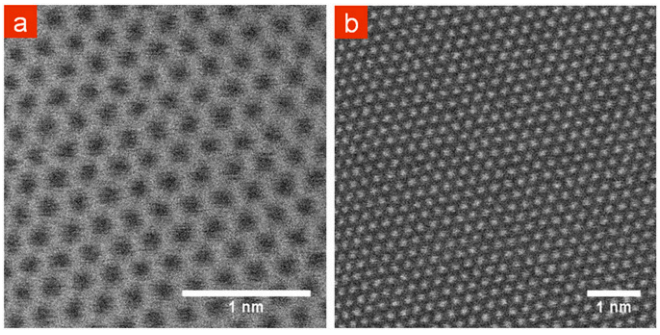

Fig. S3. (*A* and *B*) Raw STEM images of AA- and AB-stacked graphene, respectively. Stacks of three and seven similar images were cross-correlated and averaged and contrast-adjusted to generate Fig. 2 *C* and *D*.

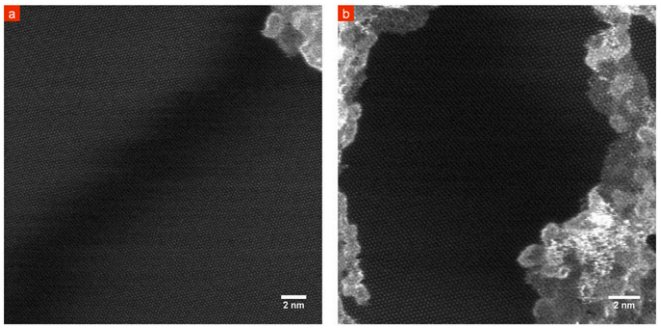

Fig. S4. (*A* and *B*) Raw STEM images of shear- and tensile-strain soliton boundaries. Three to four adjacent regions along these solitons were averaged and contrast-adjusted to generate Fig. 3 *A* and *D*.

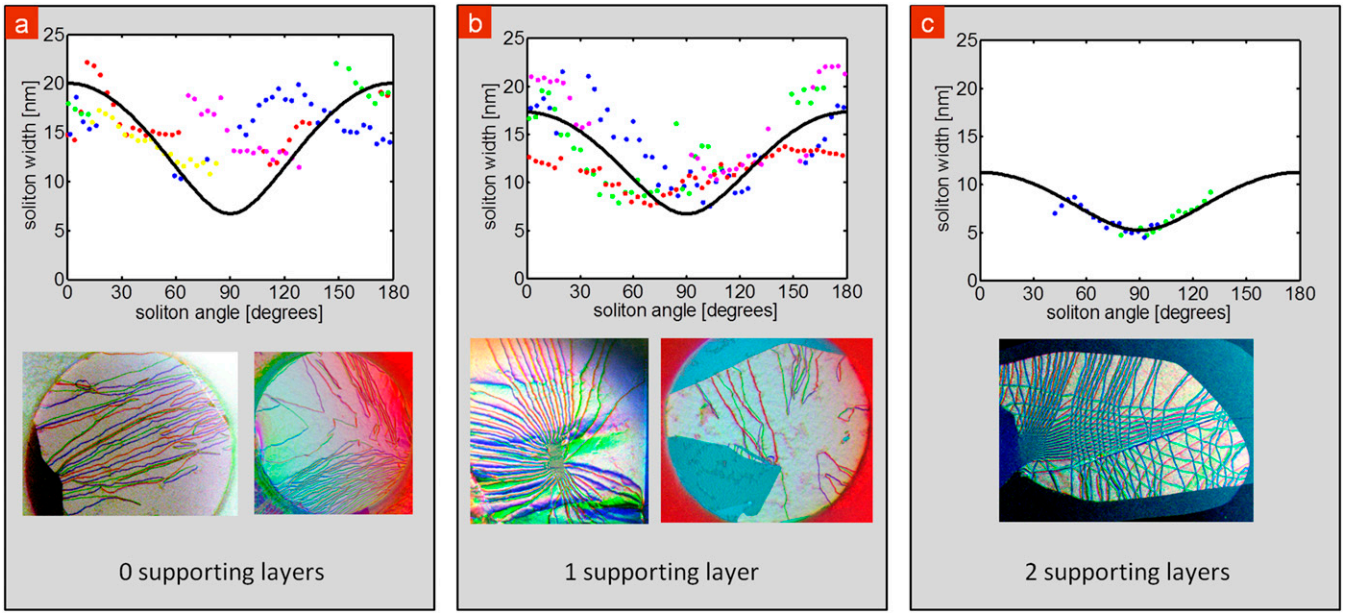

Fig. S5. DF-TEM images of soliton width as a function of angle, with corresponding composite images. For each sample, width measurements from two of the three soliton translation directions, $\Delta \boldsymbol{u}$, are shown. (*A*) Samples with freely suspended bilayer graphene show considerable variability in the measured soliton width, presumably owing to out-of plane corrugations in the graphene. (*B*) Samples with one additional graphene layer (at a non-Bernal-stacking angle) show qualitative agreement with our model, but considerable variability. (*C*) Samples with two additional supporting graphene layers show excellent agreement with our model and with the STEM width measurements.

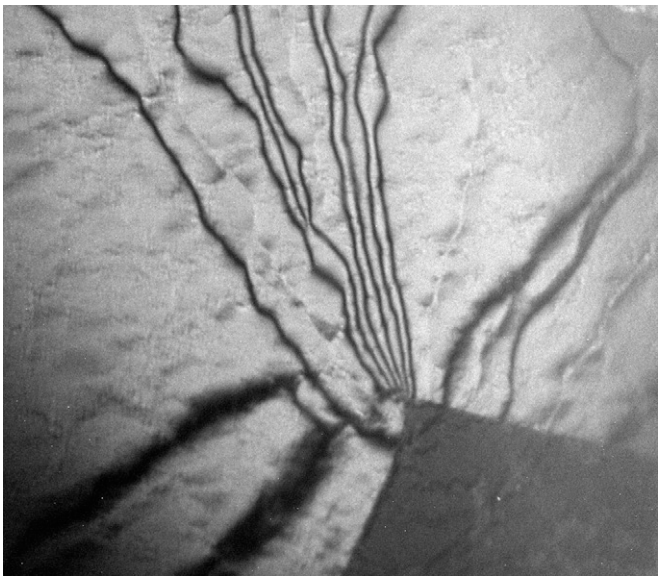

Movie S1. DF-TEM video taken from the [−2110] family of diffraction angles, showing interlayer solitons fluctuating over the course 43 min under the influence of a high-intensity electron beam (3.6×10^4 $e^- \cdot nm^{-2} \cdot s^{-1}$, 80 keV). Each frame in Movie S1 is an average of three images, each taken with a 20-s exposure.

Movie S1

Movie S2. DF-TEM video taken at 1,000 °C, under low beam intensity (80 keV, $\sim 3 \times 10^3$ $e^- \cdot nm^{-2} \cdot s^{-1}$), using an aperture to select electrons from the [−1010] family of diffraction spots, showing AB and BA domains growing and shrinking as the solitons move. At our temporal resolution, motion often appears to occur in discrete steps. Upon first heating the sample, motion was significant at 1,000 °C. Because, after heating to 1,200 °C, cooling, and reheating to 1,000 °C motion was negligible, we posit that the initial motion at 1,000 °C is primarily due to stress relaxation. Videos were cross-correlated to remove sample drift, and each video frame is an average of five 20-s exposures. Movie S2 was taken over the course of 35 min. (The isolated white pixels here and in other movies are dead pixels in the CCD that seem to move owing to the cross-correlation-based sample-drift correction.)

Movie S2

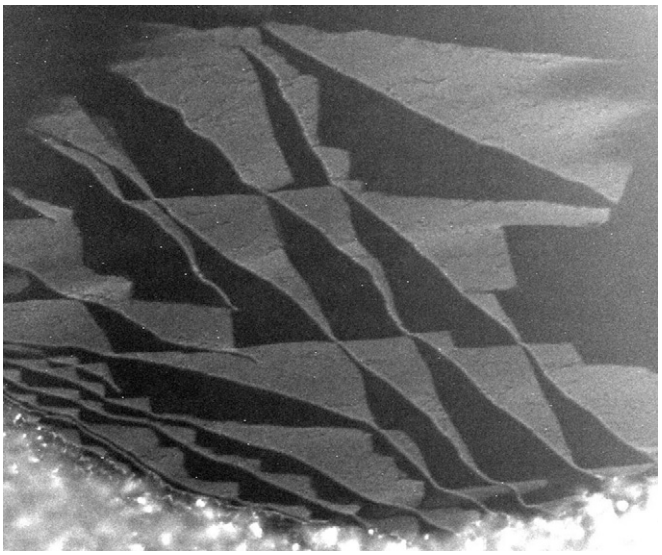

Movie S3. DF-TEM video taken at 1,100 °C, under the same conditions as Movie S2, over the course of 27 min.

Movie S3

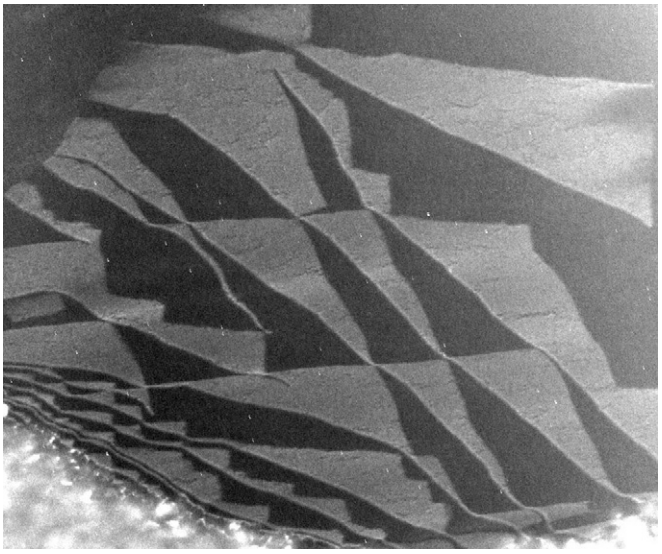

Movie S4. DF-TEM video taken at 1,200 °C, under the same conditions as Movie S2, over the course of 27 min.

Movie S4

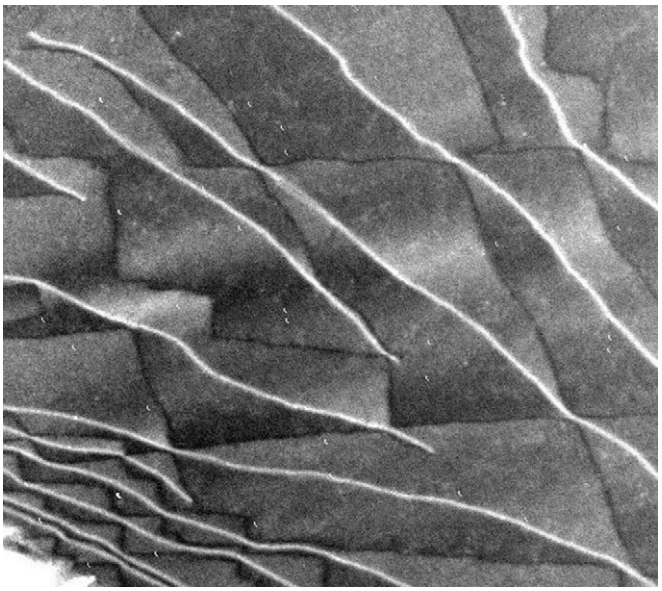

Movie S5. DF-TEM video taken at 1,200 °C over the course of 138 min using the same imaging conditions and averaging procedure as Movie S2. The sample has been tilted, leading to contrast among the domains and boundaries that appears different from that of Movies S2, S3, and S4.

Movie S5